




Article

# An Investigation into Electrolytes and Cathodes for Room-Temperature Sodium–Sulfur Batteries

Hakeem Ademola Adeoye , Stephen Tennison, John F. Watts  and Constantina Lekakou \* 

Centre of Engineering Materials, School of Mechanical Engineering Sciences, University of Surrey, Guildford GU2 7XH, UK; h.adeoye@surrey.ac.uk (H.A.A.); steve.tennison@carbontex.co.uk (S.T.); j.watts@surrey.ac.uk (J.F.W.)

\* Correspondence: c.lekakou@surrey.ac.uk; Tel.: +44-(0)1483689622

**Abstract:** In the pursuit of high energy density batteries beyond lithium, room-temperature (RT) sodium–sulfur (Na-S) batteries are studied, combining sulfur, as a high energy density active cathode material and a sodium anode considered to offer high energy density and very good standard potential. Different liquid electrolyte systems, including three different salts and two different solvents, are investigated in RT Na-S battery cells, on the basis of the solubility of sulfur and sulfides, specific capacity, and cyclability of the cells at different C-rates. Two alternative cathode host materials are explored: A bimodal pore size distribution activated carbon host AC MSC30 and a highly conductive carbon host of hollow particles with porous particle walls. An Na-S cell with a cathode coating with 44 wt% sulfur in the AC MSC30 host and the electrolyte 1M NaFSI in DOL/DME exhibited a specific capacity of 435 mAh/g<sub>S</sub> but poor cyclability. An Na-S cell with a cathode coating with 44 wt% sulfur in the host of hollow porous particles and the electrolyte 1M NaTFSI in TEGDME exhibited a specific capacity of 688 mAh/g<sub>S</sub>.

**Keywords:** Na-S batteries; liquid electrolytes; cathode hosts; activated carbon; hollow porous particles; room-temperature Na-S batteries



**Citation:** Adeoye, H.A.; Tennison, S.; Watts, J.F.; Lekakou, C. An Investigation into Electrolytes and Cathodes for Room-Temperature Sodium–Sulfur Batteries. *Batteries* **2024**, *10*, 216. <https://doi.org/10.3390/batteries10060216>

Academic Editors: Seiji Kumagai and Yu Jiang

Received: 16 May 2024

Revised: 14 June 2024

Accepted: 16 June 2024

Published: 20 June 2024



**Copyright:** © 2024 by the authors. Licensee MDPI, Basel, Switzerland. This article is an open access article distributed under the terms and conditions of the Creative Commons Attribution (CC BY) license (<https://creativecommons.org/licenses/by/4.0/>).

## 1. Introduction

Typical Li-ion batteries with graphite anodes have now reached serious limits from different viewpoints: A maximum capacity of 260 Wh kg<sup>-1</sup> of cell mass for NCA batteries [1–10]; the use of critical raw materials such as cobalt and nickel; and, of course, the key strategic and critical raw material, lithium. In the race for the electrification of transport, it is clear that there is a risk that the new era of carbon-free cities might create a lithium-dependent society, and the existing lithium deposits might be inadequate to meet the estimated huge demand.

Sulfur batteries, such as lithium–sulfur or other metal–sulfur (Me-S) batteries, comprise a sulfur cathode, which has a high theoretical specific capacity of 1675 Ah kg<sup>-1</sup> [11–13]. Furthermore, sulfur is an abundant material, non-toxic, and of low cost. However, it is also an insulator, rigid, and brittle, which is a big disadvantage as this cathode material expands to its conversion to the metal sulfide (Me<sub>2</sub>S<sub>m</sub>, for Me<sup>m+</sup> ion) at the end of discharge, such as by 70% in Li-S batteries when S<sub>8</sub> converts to Li<sub>2</sub>S [14,15]. Solutions have already been devised for these problems in Li-S batteries, where good-conductivity cathode hosts, such as carbonaceous or MoS<sub>2</sub> hosts, are employed with pores to accommodate the sulfur expansion when it converts to Me<sub>2</sub>S<sub>m</sub>. Carbonaceous or other conductive hosts include hollow particles with microporous walls [16–21], activated carbon (AC) coatings [16,22–30] or AC fabrics [16,29–34], graphene [16,35–43], or carbon nanotubes [44–50]. 1T-MoS<sub>2</sub> cathode hosts have also proved very efficient for Li-S batteries [51,52] as they trap polysulfides and reduce their shuttling effect, while also acting as electrocatalysts [52,53]. Single atom catalysts on carbon hosts also have similar effects as electrocatalysts and in reducing the polysulfide shuttling effect [54–58].

The next step in the research direction towards sulfur batteries, while pursuing the aim of replacing lithium with another metal, is to compare different metals as potential anodes. Such a comparison includes different factors: (a) The cell potential of the Me-S battery; (b) the total number of electrons transferred in the redox reaction chain; (c) the maximum expected specific capacity with respect to both anode and cathode; (d) the extent of expansion from  $S_8$  to  $Me_2S_m$  (or final sulfide in the redox reaction chain); (e) the existence of suitable liquid electrolytes for the redox reaction chain to take place in the liquid electrolyte phase at room temperature; (f) the size of the metal ion, which will affect the rate of its diffusion, especially for solid state diffusion and intercalation. Table 1 presents data with regards to these comparison factors for different investigated metals, Me.

**Table 1.** Data for key comparison factors for different metal elements, Me, in the Me-S battery.

Factor	Li <sup>+</sup>	Na <sup>+</sup>	K <sup>+</sup>	Mg <sup>2+</sup>	Ca <sup>2+</sup>	Al <sup>3+</sup>
Me <sup>m+</sup> + m e <sup>-</sup> ↔ Me						
E <sub>0</sub> (V) vs. H <sup>+</sup> /H <sub>2</sub>	-3.04	-2.71	-2.93	-2.37	-2.87	-1.66
C <sub>spec</sub> (Ah kg <sup>-1</sup> )	1168	687	487	952	744	1072
E <sub>spec</sub> (Wh kg <sup>-1</sup> )	2340	1587	1232	1875	1838	1350
Expansion (%)	73	160	280	31	73	34
Me <sup>m+</sup> size (nm)	0.18	0.23	0.30	0.17	0.23	0.14
σ <sub>Me</sub> (10 <sup>6</sup> S m <sup>-1</sup> )	11	21	14	23	29	38

Starting with the standard potential of S versus H<sup>+</sup>/H<sub>2</sub>, E<sub>0</sub> = -0.4 V, and a Li anode of E<sub>0, Li<sup>+</sup>→Li</sub> = -3.04 V versus H<sup>+</sup>/H<sub>2</sub>, a Li-S battery cell has a reference potential of 2.3 V on average for the reactions related to the high-order sulfides (Li<sub>2</sub>S<sub>4</sub> to Li<sub>2</sub>S<sub>8</sub>) and 2 V for the low-order sulfides (Li<sub>2</sub>S<sub>2</sub> and Li<sub>2</sub>S) [16,59]. Table 1 depicts that similarly good negative potentials are encountered for the following metals, from best to worst: K<sup>+</sup>/K, Ca<sup>2+</sup>/Ca, Na<sup>+</sup>/Na, Mg<sup>2+</sup>/Mg and Al<sup>3+</sup>/Al. This means that an Al-S battery would operate at similarly low potential [60] as devices with aqueous electrolytes, which makes it unsuitable for high-voltage applications. Other elements, Mn<sup>2+</sup>, Zn<sup>2+</sup>, Fe<sup>2+</sup> and Sn<sup>2+</sup> are even more unsuitable for sulfur batteries in terms of cell potential, with their standard potential versus H<sup>+</sup>/H<sub>2</sub>: E<sub>0, Mn<sup>2+</sup>→Mn</sub> = -1.18 V, E<sub>0, Zn<sup>2+</sup>→Zn</sub> = -0.76 V, E<sub>0, Fe<sup>2+</sup>→Fe</sub> = -0.44 V and E<sub>0, Sn<sup>2+</sup>→Sn</sub> = -0.13 V.

In all Me-S cells, the overall reaction considered involved the transfer of 16 electrons per S<sub>8</sub> mole: S<sub>8</sub> + 16 e<sup>-</sup> ↔ 8 S<sup>2-</sup>.

The next factor to examine is the specific gravimetric capacity, C<sub>spec</sub>, with respect to the mass of the sulfur cathode and metal anode. Table 1 demonstrates that after Li, the next high value of C<sub>spec</sub> is for aluminum, but its low cell voltage, 1.26 V (half this value in experimental data [60]), means that its theoretical energy density of both electrodes, 1350 Wh kg<sup>-1</sup>, is lower than the theoretical energy density of Me-S cells with other metal anodes in Table 1. Considering the highest C<sub>spec</sub> values in Table 1, the best metals are in the order of: Mg (best), Ca, Na, and K (worst).

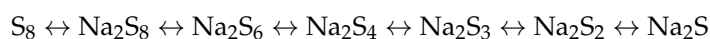
Combining an estimated cell voltage and the specific capacity data, the theoretical energy density values in Table 1 (also reported in [61]) indicate the following order for the metals, from best to worst: Mg, Ca, Na, and Al. All four of these metals also have better electronic conductivity, σ<sub>Me</sub>, than lithium, as seen in Table 1. Given the discussion on the low cell voltage of Al-S batteries, this option is excluded from further evaluation.

Looking at the sulfur expansion when converted to Me<sub>2</sub>S<sub>m</sub>, the three best Me-S options can be ordered from best to worst as: Mg (31%), Ca (73%), and Na (160%), compared to Li (73%). Hence, the best alternatives to Li-S batteries might be Mg-S, Ca-S, and Na-S batteries. Despite the low cathode expansion of Mg-S batteries, their actual performance is very weak, with extremely low cell potential below 0.8 V, huge overpotential, low specific capacity, and poor cyclability [62]. Ca-S batteries might have a better chance, but their future is still uncertain due to the lack of a suitable electrolyte, which is capable of efficient ion transfer and does not form a surface-blocking layer on Ca metal [63]. Hence, our research efforts

have concentrated on the Na-S battery, which involves the next alkali metal after lithium in the periodic table.

Despite the high expansion of the sulfur cathode in Na-S batteries, there is significant experience in high-temperature (HT) Na-S batteries, which are commercially available, operate routinely at 2 V, have a temperature of 300–340 °C, an energy density of 220 Wh/kg of cell, and a have high cyclability of over 7000 cycles [64–68]. The redox reaction chain for HT Na-S batteries comprises the conversion of  $S_8$  to  $Na_2S_x$ , with  $3.3 \leq x \leq 5$ .

Further progress has been made to devise and develop liquid electrolytes for room-temperature (RT) Na-S batteries. Following the experience of high performing Li-S batteries, it has been noticed that good electrolytes include ether-based solvents, such as the electrolyte 1M LiTFSI in DOL/DME (1,3-dioxolane/1,2-dimethoxyethane) [69] or TEGDME (tetraethylene glycol dimethyl ether) [70]. Carbonate-type solvents are not used in Li-S batteries as they exhibit side reactions with the dissolved polysulfides via a nucleophilic addition or substitution [71–75]. For this reason, carbonate electrolytes have been excluded from this study for Na-S batteries as well, to ensure best efficiency and good cyclability [76]. It has been found [77–80] that the Na-S reaction chain in ether-based electrolytes follows the sequence:



The first step in our group's research was to determine the solubility and dissolution kinetics of sulfur and the above sodium sulfides in the electrolyte solvents DOL/DME 1:1 *v/v* and TEGDME [81]. Figure 1 presents a comparison of the saturation concentration data of the sodium sulfides in these two electrolyte solvent systems against the saturation concentrations of the lithium sulfides in DOL/DME. It can be clearly seen that the lithium sulfides have 5–10 times higher solubility in DOL/DME than the sodium sulfides in the same solvent system. Furthermore, TEGDME seems to be a better solvent for  $Na_2S_x$ ,  $x = 4, 6, 8$ , than DOL/DME. The low solubility of  $Na_2S_3$  makes it more soluble in DOL/DME than in TEGDME, although its solubility is still low even in DOL/DME.

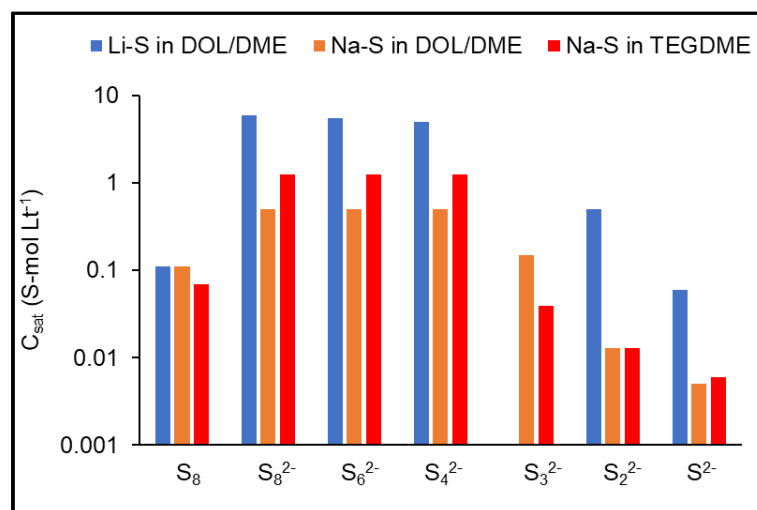


**Figure 1.** Saturation concentration,  $C_{sat}$ , diagram of sulfur, and lithium sulfides or sodium sulfides in solvents DOL/DME 1:1 *v/v* and TEGDME.

However, sulfur batteries undergo a series of parallel physical, electrochemical, and chemical processes with competing effects, some beneficial and others harmful. Hence, although the high solubility of sulfur and sulfides increases the volume of reactions and productivity rate in the liquid electrolyte phase, it also facilitates the migration of solutes away from the cathode. Modeling of ion migration in mesoporous electrodes [82,83], such as sulfur batteries [16,59], is highly linked with the cathode microstructure in terms of pore

size distribution [16,59,84,85], tortuosity [42,86,87], and how the pore sizes relate to the size of solvated and desolvated solute species [88].

For this reason, this study investigates six liquid electrolyte systems for room-temperature Na-S batteries, comprising six combinations of the two solvent systems already tested in our solubility studies, TEGDME and DOL/DME, and three salts, NaTFSI, NaFSI, and NaCF<sub>3</sub>SO<sub>3</sub>. Two alternative cathode host materials are tried, both with high specific pore volumes to accommodate the sulfur and its estimated expansion if it ultimately converts to Na<sub>2</sub>S. The first host is characterized by a bimodal pore size distribution consisting mainly of micropores. The second host is a coating containing hollow carbon nanoparticles with a microporous wall.

## 2. Materials and Methods

### 2.1. Materials and Cell Components

One mole electrolyte solutions were prepared using the following salts: NaTFSI of 99.5% purity (Solvionic, France), NaFSI of 99.9% purity (Solvionic, France), and NaCF<sub>3</sub>SO<sub>3</sub> of 99.5% purity (Solvionic, France). Solvents included TEGDME anhydrous, 99.5% (Sigma Aldrich, UK), and DOL anhydrous, 99.8% (Sigma Aldrich, UK), DME anhydrous, 99+% (Alfa Aesar™, Europe). A solvent mixture of DOL/DME 1:1 *v/v* was prepared. In summation, six electrolyte solutions were prepared and used in this study:

1M NaTFSI in DOL/DME 1:1 *v/v*;  
 1M NaTFSI in TEGDME;  
 1M NaFSI in DOL/DME 1:1 *v/v*;  
 1M NaFSI in TEGDME;  
 1M NaCF<sub>3</sub>SO<sub>3</sub> in DOL/DME 1:1 *v/v*;  
 1M NaCF<sub>3</sub>SO<sub>3</sub> in TEGDME.

Two types of cathode host materials were used. Activated carbon (AC) powder MAXSORB® MSC30 (Kansai Coke and Chemicals Co. Ltd., Japan) is henceforth denoted as AC MSC30. The Supplier specifications include BET-specific surface area, SSA<sub>BET</sub> of 3400 m<sup>2</sup> g<sup>-1</sup>, median particle diameter D50 = 60–150 μm, moisture < 5%, ash < 1%. Figure 2a presents the PSD of AC MSC30 from nitrogen adsorption experiments [89], which displays a bimodal shape with two peaks at 0.89 nm and 2.13 nm and a total specific volume of 1.6 cm<sup>3</sup> g<sup>-1</sup>. Super P carbon black (TIMCAL, Belgium) was added as a highly conductive additive, with SSA<sub>BET</sub> of 62 m<sup>2</sup> g<sup>-1</sup>, median particle diameter D50 = 40 nm, density 160 kg m<sup>-3</sup>, and sulfur content of 50–100 ppm. PVDF (polyvinylidene fluoride) of MW = 534,000 (Sigma Aldrich, UK) was used as a binder. A cathode coating was prepared with 36.4 wt% AC MSC30 host, 43.6 wt% sulfur, 10 wt% Super P carbon, and 10 wt% PVDF binder.

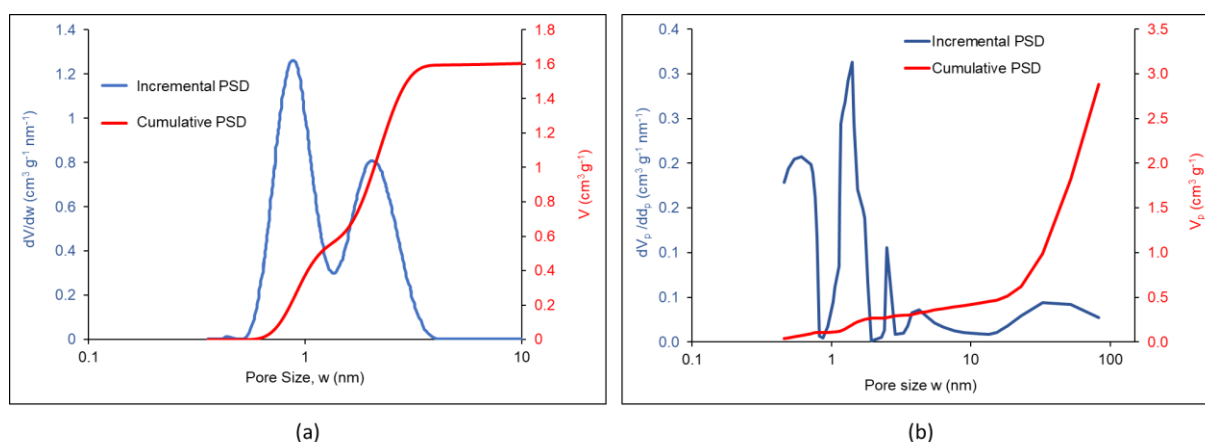


**Figure 2.** Incremental and cumulative PSDs of (a) AC MSC30 and (b) Ketjenblack EC-600JD.

The second cathode host was Ketjenblack EC-600JD (Lion Corporation, Japan), henceforth denoted as KB. It consists of highly conductive hollow carbon particles with a diameter

of 30 nm, an 80% hollow core, and a porous wall. The supplier specifies a BET-specific surface area of  $1415 \text{ m}^2 \text{ g}^{-1}$ . Figure 2b presents the PSD [16], which looks multimodal with peaks at 0.61 nm, 1.4 nm (tallest peak), 2.5 nm, 4.3 nm, and 33 nm, with the last peak being relatively broad in the range of 23–83 nm. The cumulative PSD in Figure 2b yields a total specific volume of  $2.9 \text{ cm}^3 \text{ g}^{-1}$ . From TEM and SEM images of the KB powder on suppliers' websites, one might conclude that the 23 nm peak corresponds to the core of the hollow KB particle, whereas the micropores of 0.6–2.5 nm are in the particle walls, and the 33 nm peak corresponds to pores between KB particles. A cathode coating was prepared with 46 wt% KB, 44 wt% sulfur, and 10 wt% binder.

Carbon-coated aluminum foil (MTI, USA) was used as the current collector of cathode for both cathode types. The separator for all Na-S cells was a porous Celgard 2400 membrane (Celgard, France) with a thickness of 25  $\mu\text{m}$  and a porosity of 41% [90–92].

The anode was a sodium slice freshly cut from a sodium ingot (Sigma Aldrich, UK), kept in a paraffin bottle, and used immediately in cell fabrication in the argon-filled glovebox because it is classified as water-react 1 (i.e., it reacts vigorously with water).

## 2.2. Methods

The cathode host and sulfur powders were dried at 50 °C and mixed together at the required proportion. The powder mixture was ground manually in a mortar and pestle for about an hour. The powder mix was placed in a sealed foil envelope on a tray and heated in an oven at 155 °C for 3 h. The sulfur-impregnated host mixture was ground in a pestle and mortar for 30 min., after Super P carbon black was added to the mixture with the AC MSC30 host. The ground mixture was dispersed in an N-methyl-2-pyrrolidone (NMP) solvent under magnetic stirring. PVDF binder was dissolved in a small amount of NMP at 60 °C for 30 min and added to the mixture. The slurry was left under magnetic stirring, slowly evaporating the NMP until a creamy paste was formed. This paste was coated onto the current collector foil using a dogbone tool set at a gap of 250  $\mu\text{m}$  [93,94]. The fabricated cathode coating was allowed to dry for about a week at room temperature. Cathode discs of 19.2 mm diameter were hole-punched for coin cells.

All anode and battery cell fabrication took place in an argon-filled glovebox with less than 0.5 ppm moisture and oxygen. With regards to the anode, a piece of the sodium ingot (~1 cm  $\times$  1 cm  $\times$  5 cm) was brought off the jar in the glovebox and sliced with a hand scraper to 1 mm thickness across the length. The sliced part was placed on a metal plate for flattening to 0.75 mm. This sodium film was hole-punched to a disc of 19.2 mm diameter and used immediately in cell fabrication. Separator discs of 25 mm diameter were also hole-punched.

Cathode, current collector, and anode discs were wetted with electrolyte and assembled in customized coin cells with cases made of 316 stainless steel [93,94]. Electrolyte was added at the specified electrolyte-to-sulfur mass ratio, E/S, where three E/S ratios were investigated for each type of cell: 6, 10, and 16  $\mu\text{L}/\text{mg}_\text{S}$ . Each cell was left to rest for 2 h in the glovebox before testing [95].

Each battery cell was subjected to electrical impedance spectroscopy (EIS) in the range of 10 mHz to 1 MHz, after cell fabrication (pre-cycling) and after the sequence of 65 test cycles as follows: Galvanostatic discharge–charge cycles in the potential range of 0.5 to 3 V, following a schedule of C-rates according to the sequence: 5 cycles at 0.05 C, 5 cycles at 0.1 C, 10 cycles at 0.2 C, 10 cycles at 0.5 C, 30 cycles at 1 C, and 5 cycles at 0.1 C. All testing for all cells took place at room temperature, with a measured laboratory temperature of 20 °C.

Microstructural characterization of cathode coatings was conducted via SEM (scanning electron microscopy)/EDX (energy dispersive X-ray spectroscopy) using an HR-SEM JEOL-7100 F instrument (JEOL Ltd., Tokyo, Japan).

### 3. Results

#### 3.1. Results of Electrochemical Testing

Starting from the first five cycles at 0.05 C, Figure 3 presents the results of the best discharge (i.e., with the highest specific capacity at discharge) from each type of cell with a cathode consisting of 44 wt% S in host AC MSC30. Figure S1 (included in the Supplementary Information (SI) File) presents the specific capacity at discharge for a cycling schedule at different C-rates for each type of cell. It can be seen that the cells with electrolyte in the DOL/DME solvent system exhibit negligible specific capacity after the first few cycles at 0.05 C, which might be attributed to the low solubility of sulfides in DOL/DME compared to TEGDME [81]. Even the cells with electrolyte in the TEGDME solvent exhibit negligible specific capacity at the 1 C-rate. Hence, the next step was to cycle the best cells at low C-rates, i.e., starting with 5 cycles of galvanostatic discharge–charge cycles at 0.05 C and continuing cycling at 0.1 C. These best cells were those with TEGDME-based electrolytes, where TEGDME seems to be the best solvent and has the best E/S ratio, according to the results of Figures 3 and S1. The results are presented in Figure 4.

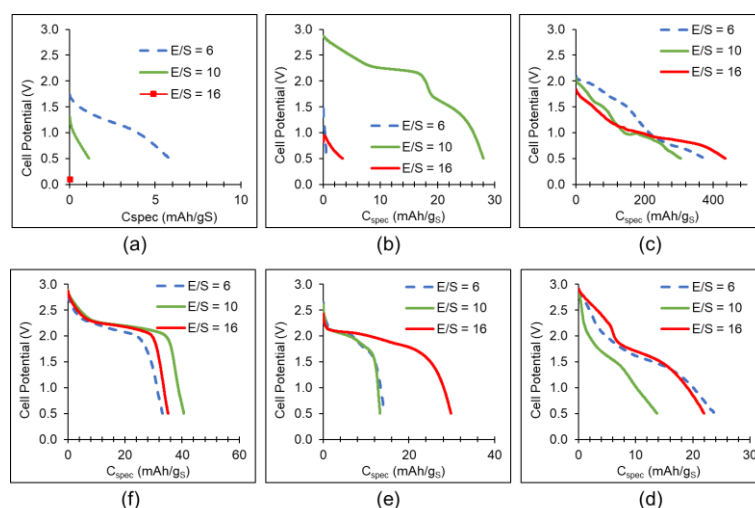


**Figure 3.** The best galvanostatic discharge curves (i.e., with the highest specific capacity at discharge) from the first 5 cycles at 0.05 C of Na-S cells with cathode of 44 wt% sulfur with host AC MSC 30, for all six electrolytes and different E/S ratios (in  $\mu\text{L}/\text{mg}_\text{S}$ ): (a) 1M NaTFSI in DOL/DME; (b) 1M NaTFSI in TEGDME; (c) 1M NaFSI in DOL/DME; (d) 1M NaFSI in TEGDME; (e) 1M NaCF<sub>3</sub>SO<sub>3</sub> in DOL/DME; (f) 1M NaCF<sub>3</sub>SO<sub>3</sub> in TEGDME.

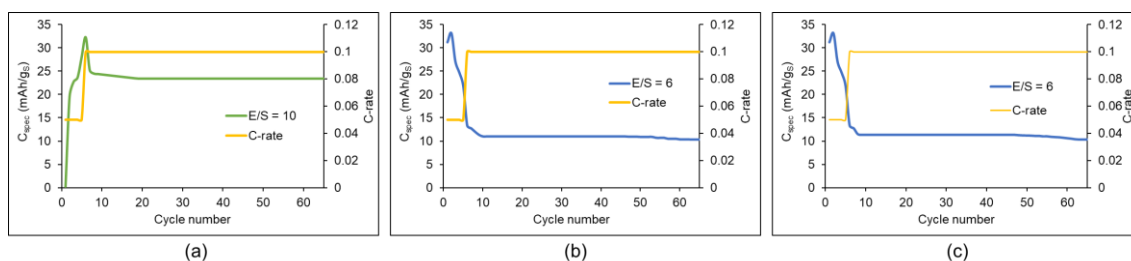


**Figure 4.** Specific capacity at discharge versus cycle number in the galvanostatic discharge–charge tests of Na-S cells with cathode of 44 wt% sulfur with host AC MSC 30, for different electrolytes and the best E/S ratio (in  $\mu\text{L}/\text{mg}_\text{S}$ ) for each electrolyte: (a) 1M NaTFSI in TEGDME; (b) 1M NaFSI in TEGDME; (c) 1M NaCF<sub>3</sub>SO<sub>3</sub> in TEGDME.

Looking at the results of Figures 3, 4, and S1, it can be seen that the discharge with the longest capacity is encountered not always in the first cycle but in most cases in the second, third, or fourth cycle. Looking at the effect of E/S ratio, electrolyte-lean cells ( $E/S =$

6  $\mu\text{L}/\text{mg}_\text{S}$ ) exhibited the best specific capacity in Figure 3a,d, although the cell in Figure 3a with the DOL/DME-based electrolyte died very quickly after the first couple of cycles (Figure S1a).  $E/S = 10 \mu\text{L}/\text{mg}_\text{S}$  is the best  $E/S$  ratio for the cells in Figure 3b,f, both with TEGDME-based electrolytes. In general, a low  $E/S$  ratio is beneficial to the discharge capacity of Li-S cells because it would dissolve a smaller amount of sulfur and sulfides and impede their migration to the anode; however, a low  $E/S$  ratio may also mean poor wetting of the cathode, and low dissolution of sulfur and sulfides would slow down the redox Li-S reactions, which would reduce cell capacity. Hence, the optimum  $E/S$  ratio depends on which of these two opposing effects dominates. A highly electrolyte-flooded cell may trigger further surprising effects: Some cells with  $E/S = 16 \mu\text{L}/\text{mg}_\text{S}$ , notably the case of 1M NaTFSI in DOL/DME in Figure 3a, after cell fabrication and while resting for 2 h before any testing is conducted so that the electrolyte has the chance to impregnate all cell porous parts and parts interfaces, experience a series of processes that may result in a huge rise of cell resistance leading to immediate discharge below 0.5 V in the first GDC cycle (Figure 3a): A large amount of electrolyte dissolves much sulfur that migrates from the micro- to meso- and macropores, exceeding the saturation concentration and leading to the formation of heavy, solid sulfur deposits on the cathode surface that raise the cell resistance, sometimes to very high values [95]. A smaller  $E/S$  ratio would yield less sulfur dissolution, which would disturb less of the initial sulfur distribution in the cathode host and avoid the formation of thick insulator layers.

Comparing cells of different electrolytes at the best respective  $E/S$  ratio, Figure 3b,f exhibit high voltage plateaus, comparable to Li-S batteries, with electrolyte 1M NaTFSI in TEGDME and 1M  $\text{NaCF}_3\text{SO}_3$  in TEGDME, and  $E/S = 10 \mu\text{L}/\text{mg}_\text{S}$  in both cases. The good cyclability of the cell with 1M NaTFSI in TEGDME and  $E/S = 10 \mu\text{L}/\text{mg}_\text{S}$  is noted in Figure 4a and Figure S1b in SI. Cells with electrolyte 1M NaTFSI in DOL/DME exhibit high specific capacity, reaching a maximum of 435  $\text{mAh}/\text{g}_\text{S}$  in Figure 3c, which however falls to zero after the first discharge, as can be seen in Figure S1c. Hence, we reached the conclusion from Figure 3 and Figure S1 that, overall, cells with electrolytes using the TEGDME solvent exhibited more stable behavior than those with the DOL/DME solvent system.

Hence, these cells with TEGDME = based electrolyte and the best  $E/S$  ratio, respectively, were cycled at low C-rates, and the cyclability results are presented in Figure 4. Figure 4 illustrates that the Na-S cell with the electrolyte 1 M NaTFSI in TEGDME exhibits the best cyclability.

Figure 5 presents the Nyquist plots from the EIS test data of all cells after they have been fabricated, pre-cycling (EIS-pre), and selective cells post-cycling, i.e., after the full sequence of the 65 cycles of galvanostatic discharge–charge presented in Figure S1. The equivalent-in-series resistance (ESR) can be determined in each Nyquist plot as the sum of the  $Z_{\text{re}}$  values from the first intercept of the Nyquist curve with the  $Z_{\text{re}}$  axis and the cords of all Nyquist semicircles, before the Nyquist curve might rise for the Warburg part at low frequencies. Figure 5a, referring to a cell with electrolyte 1M NaTFSI in DOL/DME and  $E/S = 10 \mu\text{L}/\text{mg}_\text{S}$ , presents two semicircles to a high combined ESR resistance and no Warburg part at medium and low frequencies. This can be attributed to the heavy precipitation of any dissolved sulfur that may continuously dissolve, move to the cathode surface, and precipitate [95] creating thick insulator layers that impede any electrolyte diffusion at low frequencies; hence, no diffusion tail exists in the Nyquist plot at low frequencies. For the same electrolyte salt, 1M NaTFSI, but in TEGDME solvent, Figure 5b exhibits diffusion tails for  $E/S = 6$  and  $10 \mu\text{L}/\text{mg}_\text{S}$ , which may be attributed to the lack of thick sulfur deposits due to the better dissolution of sulfur in this electrolyte system. The noise in the low frequency region of some Nyquist plots in Figure 5 might be due to discontinuities of such precipitated sulfur or sulfide layers on the cathode surface, separator, and anode in some cells [16,95]. The as-fabricated cell in Figure 5b with  $E/S = 16 \mu\text{L}/\text{mg}_\text{S}$  displays a very low ESR value, which might be attributed to the full dissolution of sulfur by the large amount of electrolyte and its transport to parts of the cell in the gap at the periphery of the separator excess outside the electrode discs. This would then support the

low specific capacity of this cell in Figure 3b and Figure S1b, especially in the first cycle (Figure S1b).

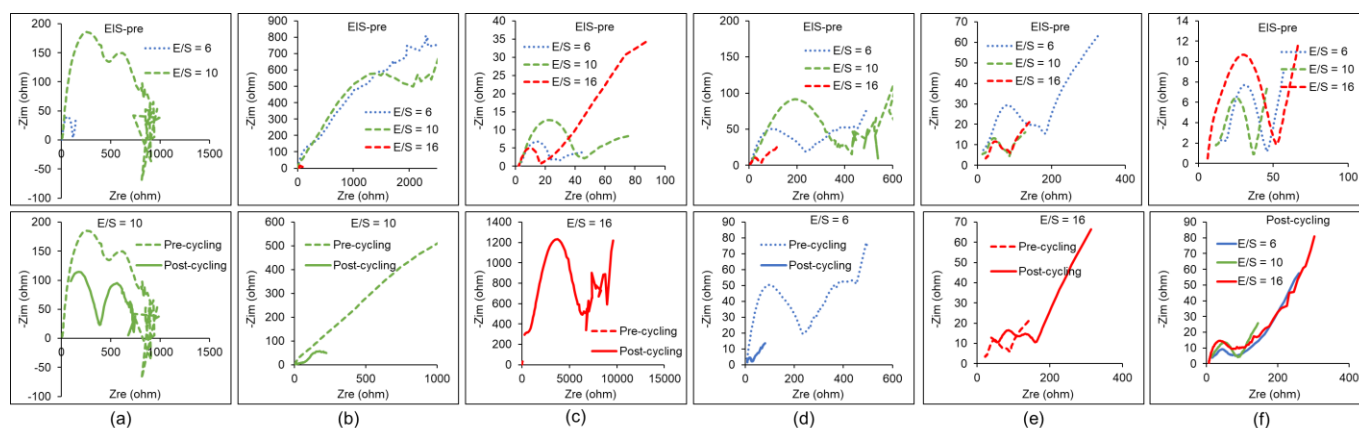


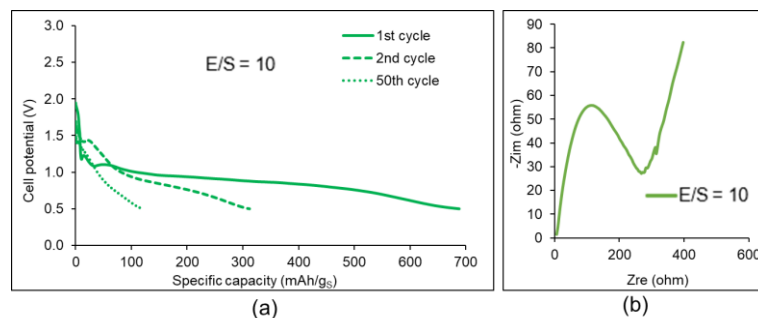
**Figure 5.** Nyquist plots from the EIS tests of Na-S cells with cathode of 44 wt% sulfur with host AC MSC 30, for all six electrolytes and different E/S ratios (in  $\mu\text{L}/\text{mg}_\text{S}$ ): (a) 1M NaTFSI in DOL/DME; (b) 1M NaTFSI in TEGDME; (c) 1M NaFSI in DOL/DME; (d) 1M NaFSI in TEGDME; (e) 1M NaCF<sub>3</sub>SO<sub>3</sub> in DOL/DME; (f) 1M NaCF<sub>3</sub>SO<sub>3</sub> in TEGDME.

It can be seen that, in most cases, high ESR is generated during cycling. This high resistance is the cause of cell death during cycling and negligible specific capacity at 1 C in Figure S1. Of particular interest is the cell of initially high capacity in Figure 3c, which falls abruptly after the first cycle in Figure S1c due to an ESR value of 9000 ohm in Figure 5c. On the other hand, the postmortem ESR value for the cell in Figure 3b falls to 200 ohm (from an initial pre-cycling ESR value of 2400 ohm) in Figure 5b, which explains the good cyclability of this cell in Figure 4b. The high ESR values in some cells can be attributed to insulator layers of precipitated sulfur species, especially in the case of the low sulfide solubility in DOL/DME-based electrolytes in Figure 5a,c post-cycling or in electrolyte-lean cells with  $E/S = 6 \mu\text{L}/\text{mg}_\text{S}$ .

Electrolyte 1M NaTFSI in TEGDME has been selected for the next step of investigation for the following reasons: (a) The high solubility of sulfides in TEGDME as depicted in Figure 1; (b) the high voltage plateau as displayed in Figure 3b; and (c) the good cyclability of the corresponding Na-S cell as shown in Figures 4a and S1b in SI. An Na-S cell was fabricated with this electrolyte and a coating cathode of 44 wt% sulfur in a host of hollow particles with porous walls.

The results of the electrochemical testing of this cell are presented in Figure 6. Figure 6a demonstrates a high specific capacity of 688 mAh/g<sub>S</sub> at first discharge but generally a low plateau around 1 V. The specific capacity is reduced in the second discharge and thereafter, although a region of higher voltage around 1.5 V is displayed at the start of the second discharge in Figure 6a. After further cycling at 0.1 C, the cell yielded a specific capacity of 64 mAh/g<sub>S</sub> at 0.1 C in the 65th cycle, which is higher than any of the specific capacity values in the same cycle for any cells in Figure 4.

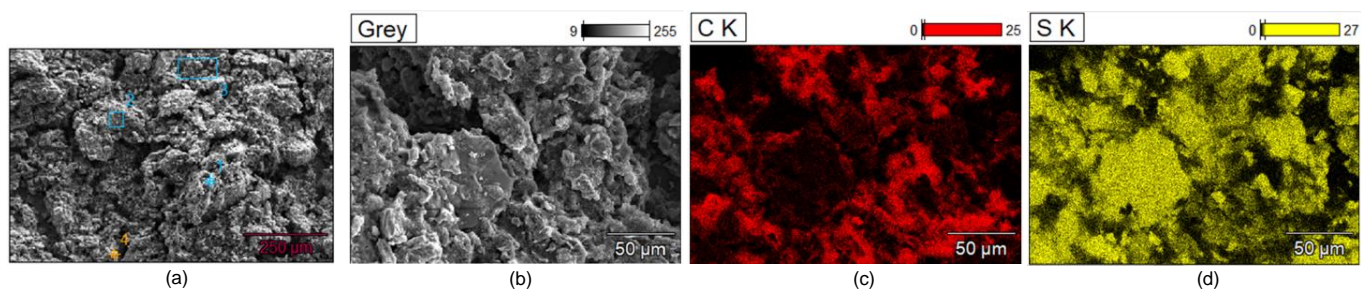




**Figure 6.** Results of the electrochemical tests of Na-S cells with cathode of 44 wt% sulfur with host KB and electrolyte 1M NaTFSI in TEGDME at E/S = 10  $\mu\text{L}/\text{mg}_\text{S}$ : (a) first, second and fiftieth galvanostatic discharges at 0.05 C; (b) Nyquist plot from the EIS test.

### 3.2. Results of Material Characterization

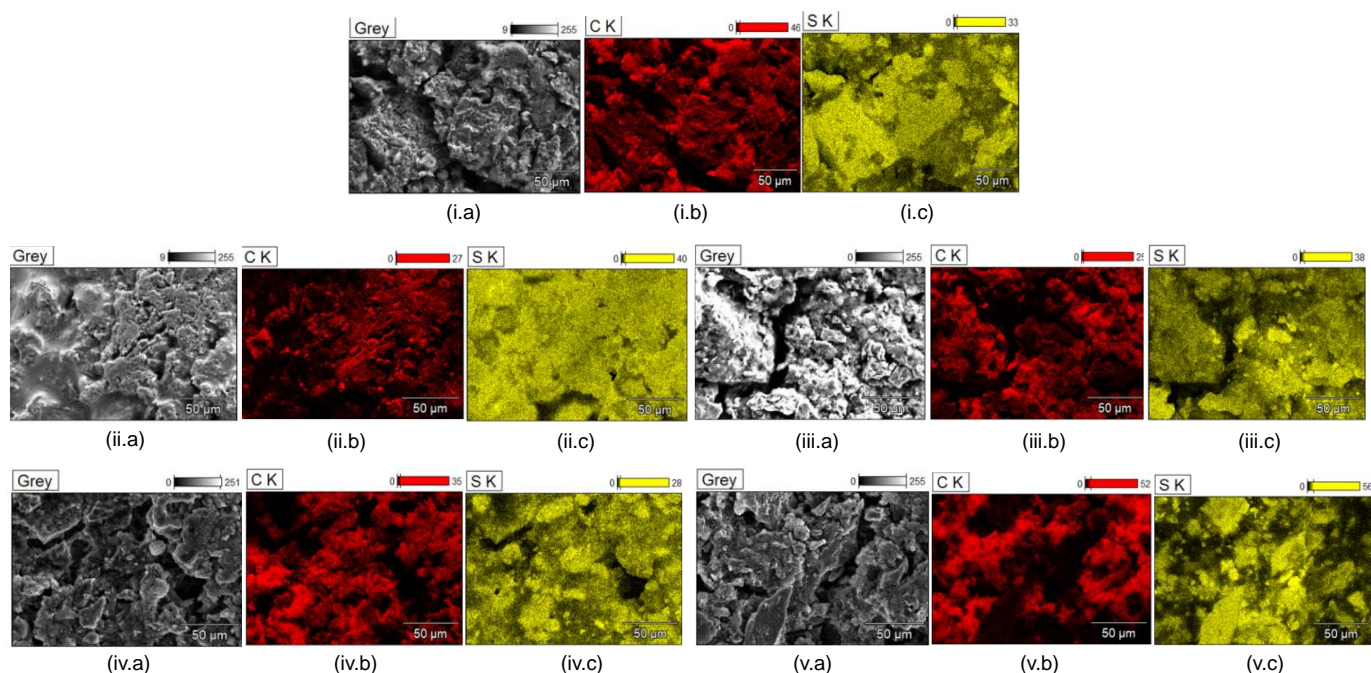
Figure 7a presents an SEM image of the as-fabricated cathode coating based on the AC MSC30 host, which exhibits crack formation, as is characteristic of many sulfur cathode coatings, e.g., in the commercial NANOMYTE<sup>®</sup> BE-70E coating [69]. Figure 7a shows coating domains as agglomerates of 250–500  $\mu\text{m}$  diameter surrounded by cracks of 15–30  $\mu\text{m}$  width, similarly to the microstructure domain and crack size in the NANOMYTE<sup>®</sup> BE-70E coating [69]. EDX analysis of the elemental composition of Figure 7b reveals that the sulfur domains in Figure 7d spread beyond the underneath carbon host structure in Figure 7c; further measurements led to an estimated excess sulfur layer of 7 nm over the external surface of carbon particles.



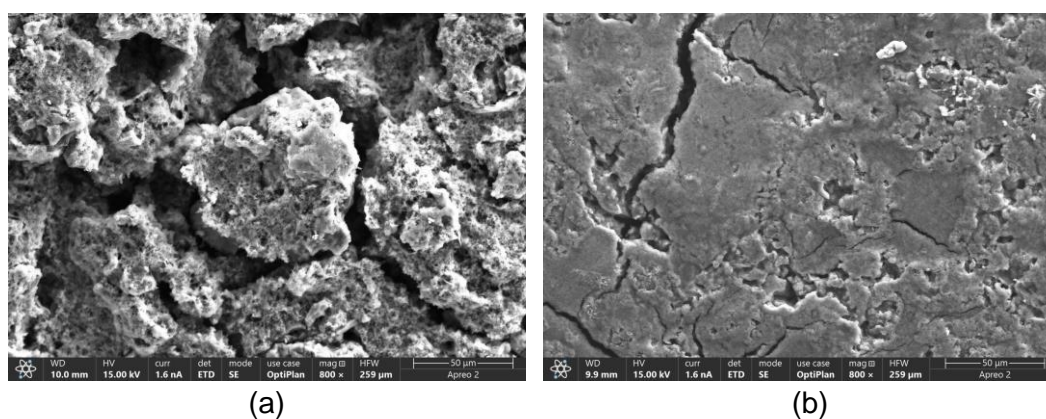
**Figure 7.** SEM images (a,b) and EDX element map of (c) carbon and (d) sulfur of the as fabricated cathode coating with 44 wt% sulfur and host AC MSC30.

Figure 8 displays the postmortem SEM/EDX results for the same cathode. Comparing Figure 8i (from cell with electrolyte 1M NaTFSI in TEGDME) to Figure 7, it can be seen that sulfur and sulfide compounds are massively deposited on the cathode surface in a fully spread manner without any gaps. Homogeneously deposited sulfur is also observed in Figure 8ii (from cell with electrolyte 1M NaTFSI in DOL/DME at E/S = 6  $\mu\text{L}/\text{mg}_\text{S}$ ). Furthermore, there is an impression of crack formation in the carbon host in all cells in Figure 8, which might be due to the sulfur expansion and contraction during cycling.

Figure 9a presents an SEM image of the as-fabricated cathode coating based on the KB host, which exhibits crack formation, creating model coating domains of 100–200  $\mu\text{m}$  diameter surrounded by cracks of 20–30  $\mu\text{m}$  width, similarly to the microstructure in Figure 7 and in agreement with the microstructures of similar cathode coatings in [95]. Figure 9b displays the postmortem SEM image for the same cathode, where, compared to Figure 9a, it can be seen that there are extensive flat deposits on the cathode.



**Figure 8.** Postmortem SEM images, (a) and EDX element maps of (b) carbon and (c) sulfur of the cathode coating with 44 wt% sulfur and host AC MSC30, after cell testing and cycling. Na-S cells with the electrolytes: (i) 1M NaTFSI in TEGDME at E/S = 10  $\mu\text{L}/\text{mg}_\text{S}$ ; (ii) 1M NaFSI in DOL/DME at E/S = 6  $\mu\text{L}/\text{mg}_\text{S}$ ; (iii) 1M NaFSI in DOL/DME at E/S = 16  $\mu\text{L}/\text{mg}_\text{S}$ ; (iv) 1M NaFSI in TEGDME at E/S = 6  $\mu\text{L}/\text{mg}_\text{S}$ ; (v) 1M NaFSI in TEGDME at E/S = 10  $\mu\text{L}/\text{mg}_\text{S}$ .



**Figure 9.** SEM images of the KB-based cathode with 44 wt% sulfur: (a) as-fabricated cathode; (b) postmortem microstructural characterization of cathode, after cell testing and cycling. Na-S cell with electrolyte 1M NaTFSI in TEGDME at E/S = 10  $\mu\text{L}/\text{mg}_\text{S}$ .

#### 4. Discussion

AC MSC30 was a model cathode host material used in the screening of electrolytes in this study for the following reasons: (a) It is an AC material with a high specific pore volume for this type of cathode host, allowing for maximum sulfur loading and its expansion in an Na-S cell. (b) It is a microporous material with a high specific surface area, where the micropores may reduce the shuttling effect while the large specific area will improve the rate of electron transfer. Taking into account the total specific pore volume of 1.6  $\text{cm}^3 \text{g}^{-1}$  of AC MSC30 (Figure 2a), it would be possible to load this host material up to 76 wt% sulfur. However, taking into account the estimated maximum expansion of 160% (Table 1), the 43.6 wt% sulfur concentration in the cathode coating (including 36.4 wt% AC MSC30) was designed as the maximum sulfur amount that would allow the 160% expansion if the full

amount was to be converted to  $\text{Na}_2\text{S}$ . Regarding the second investigated cathode host, it offers the additional advantage of hollow porous KB particles, where the possible retention of sulfur and sulfides in the hollow particle core offers an additional reason for reducing the shuttling effect. KB has a total specific volume of  $2.9 \text{ cm}^3 \text{ g}^{-1}$ ; with the same amount of sulfur as in the AC MSC30 host, 44 wt% of the cathode coating, after a maximum 160% expansion of sulfur at the end of discharge, 55% of the KB pore volume is still free. Hence, the KB host can more than accommodate the sulfur expansion in Na-S batteries for 44 wt% S in the cathode. However, these calculations are based on the overall pore volume.

Experimental [32] and simulation studies [16] have shown that micropores are filled with sulfur at a pore volume percentage ranging from 50% (micropores of 0.64 nm) to 100% (micropores equal to or greater than 0.9 nm). In such cases, the embedded sulfur may follow two routes during the operation of an Na-S battery: Either to be dissolved in the electrolyte and in that form might leach out of the micropores in the form of sulfur or sulfides, as it has indeed been found in simulations of the discharge phase of a Li-S battery cell using a digital twin that took into account the pore size distribution of the cathode and inter pore species transport [16,59]; or to convert to sodium sulfides following the chain of electrochemical reactions with  $\text{Na}^+$  ions slowly diffusing in the micro- and ultramicropores. In the latter case, two hypotheses are valid. In the first hypothesis, the  $\text{Na}^+$  ion diffusion in the ultramicropores is very slow, and the reaction chain never reaches the final stage of  $\text{Na}_2\text{S}$  formation or  $\text{Na}_2\text{S}$  is formed in a one-step reaction [96] from sulfur, but only a small proportion of the sulfur impregnated in the ultramicropores is converted to  $\text{Na}_2\text{S}$ . In both cases, only limited expansion of active material takes place in the micropores, not reaching the maximum 160% expansion. In the second hypothesis, possibly valid in the larger micropores where  $\text{Na}^+$  ion diffusion might be easier, the expected conversion and expansion take place, resulting in crack formation and fragmentation of the carbon host.

A third very important mechanism taking place in Na-S batteries is the migration of soluble sulfur and sulfides to the anode during discharge and their shuttling between the anode and cathode during charge [16]. Figures S2–S4 (included in the SI File) present photographs of the anode, cathode, and separator (surface opposite cathode) of the opened Na-S cells postmortem after all the electrochemical testing and 65 cycles of galvanostatic discharge–charge. A quick comparison illustrates that orange ( $\text{Na}_2\text{S}_4$ ) and brown ( $\text{Na}_2\text{S}_6$  and  $\text{Na}_2\text{S}_8$ ) deposits are encountered on the anode and separator of most Na-S cells with TEGDME electrolyte, which is a better solvent for  $\text{Na}_2\text{S}_4$ ,  $\text{Na}_2\text{S}_6$ , and  $\text{Na}_2\text{S}_8$  than the DOL/DME solvent system, as shown in Figure 1. On the other hand, yellow deposits on the separator and anode of the DOL/DME solvent system indicate sulfur migration towards the anode, as DOL/DME is a little better solvent for sulfur than TEGDME, as indicated in Figure 1. In any case, sulfur and sulfide migration to the anode depletes the active material from the cathode and further may cause side reactions of the sulfides at the anode during charge [97–99].

The elimination of sulfide migration away from the cathode in Na-S cells with electrolyte 1M NaFSI in DOL/DME, as illustrated in Figure S3a, seems to allow for a significant degree of sulfur conversion in the first discharge in Figure 3c but is not repeated in the following cycles as shown in Figure S1c due to the generation of high ESR as depicted by the post-cycling EIS data in Figure 5c. The reason for this might be fragmentation of the carbon cathode host during the high sulfur conversion and expansion in the first discharge, some evidence of which seems to be exhibited in the EDX carbon map of Figure 8(ii.b).

Looking into the question of why this high specific capacity in the first discharge is exhibited only in the cell with the electrolyte 1M NaFSI in DOL/DME and not in the other cells with the salts of NaTFSI or  $\text{NaCF}_3\text{SO}_3$  in the same DOL/DME solvent system. This may be due to a relatively higher transference number of  $\text{Na}^+$  ions of NaFSI in DOL/DME if it is assumed that the sodium electrolytes behave similarly to the corresponding lithium electrolytes, where it was found that  $\text{Li}^+$  ions of LiFSI in DOL/DME have a higher transference than  $\text{Li}^+$  ions of LiTFSI in DOL/DME [100,101].

Looking into the test data of the Na-S cells with the TEGDME electrolyte solvent in Figure 3b,d,f, they all exhibit relatively higher cell potential, which might be explained by the higher solubility of sulfides in TEGDME, which facilitates the reaction chain in the liquid solution phase with easier  $\text{Na}^+$  ion transport. From those, the cell with the electrolyte 1M NaTFSI in TEGDME exhibits the best cyclability in Figure 4b.

A review of the literature reveals a variety of non-hollow cathode hosts and electrolyte systems employed for RT Na-S battery cells, where in many cases, special cycling schedules or formation cycles were applied to improve performance. In sulfur non-porous solid particle cathode hosts, controlling the areal density of the coating allows for large interparticle voids that allow for the required sulfur expansion. RT Na-S cells with 50 wt% S—graphite cathode and electrolyte 1M  $\text{NaCF}_3\text{SO}_3$  in DOL/DME 1:1 *v/v* were cycled at 0.1 C, with charging galvanostatically up to 2.3 V (up to 200 mAh/g<sub>S</sub>), followed by constant voltage charge for one hour (adding 250 mAh/g<sub>S</sub> more), up to 40 cycles, at which point the discharge capacity fell to 50 mAh/g<sub>S</sub> with clear evidence of shuttling effects over all 40 cycles [102]. In another study, RT Na-S cells with a very thin (14 μm) cathode of 27 wt% S-AC (AC BP-20 Kuraray,  $\text{SSA}_{\text{BET}} = 1929 \text{ m}^2 \text{ g}^{-1}$ , total specific volume of  $0.86 \text{ cm}^3 \text{ g}^{-1}$ , pore size of 1.33 nm [103]), liquid electrolyte 1M  $\text{NaCF}_3\text{SO}_3$  in TEGDME, and a solid electrolyte separator non-porous  $\beta''\text{-Al}_2\text{O}_3$  disc of 1 mm thickness were cycled galvanostatically for 40 cycles, starting with a very low C-rate of 1/128 C, doubling it every four cycles to a maximum of 0.5 C, where they reached a capacity of 560 mAh/g<sub>S</sub> in the 19th cycle at 0.5 C [104]. In general, the need for slow cycling or the presence of low voltage discharge curves is associated with the active material being in the solid phase, either because of the low solubility of the electrolyte or encapsulation in very small micropores [84,85,105]. The low solubility of sulfides in DOL/DME [81] explains the low voltage discharge curves in Figure 3a,c in this study. The sodium sulfides experience lower solubility even in TEGDME compared to the solubility of lithium sulfides in the usual electrolyte DOL/DME used in Li-S batteries (Figure 1), while  $\text{Na}_2\text{S}_3$ ,  $\text{Na}_2\text{S}_2$ , and  $\text{Na}_2\text{S}$  are almost insoluble in either DOL/DME or TEGDME (Figure 1). For this reason, the last two redox reaction steps ( $\text{Na}_2\text{S}_3$  to  $\text{Na}_2\text{S}_2$  and  $\text{Na}_2\text{S}_2$  to  $\text{Na}_2\text{S}$ ) may be assumed to take place in a solid or semi-solid state in the present and other studies in RT Na-S batteries.

Other studies include specific additives to the electrolyte to modify the solid electrolyte interface (SEI) at the Na anode or specific separator layers to impede the shuttling of polysulfides [76]. Our own solution to reduce the shuttling of polysulfides was to choose a cathode host with hollow carbon particles (with microporous walls), which have a previous history of reducing the migration of sulfides to the anode and their shuttling in Li-S batteries [16]. For this RT Na-S cell, electrolyte 1M NaTFSI in TEGDME was employed given the better dissolving capacity of TEGDME with regards to sodium sulfides (Figure 1) and the better cyclability of cells with this electrolyte in Figure S1. This seems to be justified by the high specific discharge capacity of this cell in the first discharge cycles, as depicted in Figure 6a. However, a certain degree of sulfide migration from the micropores to the mesopores and from the cathode side near the current collector to the separator is also encountered, as illustrated by the deposits on the inner surface of the cathode (facing the separator) in Figure 9b and also predicted in Li-S batteries with the same cathode in [16]. PAN-S (polyacrylonitrile-sulfur) cathodes provide a solution for eliminating the shuttling of polysulfides and offer a possible future direction in the research and development of efficient sulfur batteries [106,107].

## 5. Conclusions

This investigation into batteries beyond lithium focused on room-temperature Na-S batteries, combining two low-cost and abundant element electrodes, a high specific energy density sulfur cathode and a sodium anode, with a combined electrode (S and Na) theoretical energy density of  $1587 \text{ Wh kg}^{-1}$ , with room-temperature liquid electrolytes. Six different electrolyte systems have been tested in RT Na-S cells. A cathode coating with 44 wt% sulfur in an AC MSC30 host yielded the highest specific capacity of 435 mAh/g<sub>S</sub> in

a 0.05 C discharge of an Na-S cell with electrolyte 1M NaFSI in DOL/DME 1:1 *v/v*; this capacity fell to a negligible value immediately after the first discharge due to the generation of high ESR that created huge resistance-related voltage differences. The reason for the high ESR values of Na-S cells with DOL/DME-based electrolyte after cell cycling is the poor solubility of sulfides in this electrolyte, which yields thick deposited layers of insulating sodium sulfides and sulfur on the cathode surface.

The same electrode coating presented very good cyclability and a high cell voltage plateau at discharge in an Na-S cell with the electrolyte 1M NaTFSI in TEGDME, but a lower specific capacity of 28 mAh/g<sub>S</sub>, due mainly to the migration of soluble sulfides from the cathode to the anode, as TEGDME is a better solvent for them than DOL/DME. This better solubility avoids the generation of thick precipitated sodium sulfide layers on the cathode surface and rise in ESR but allows for easier shuttling of the soluble sulfides between the cathode and anode.

Hence, while 1M NaTFSI in TEGDME is the recommended electrolyte from this study, an alternative cathode host was investigated with the ability to trap the soluble sulfides in the cathode. A second cathode coating with 44 wt% sulfur in KB host of hollow nanoparticles with porous walls yielded a maximum specific capacity of 688 mAh/g<sub>S</sub> in a 0.05 C discharge of an Na-S cell with electrolyte 1M NaTFSI in TEGDME. Although TEGDME is a good solvent for sulfides, their migration to the anode was reduced by physically trapping them in the hollow KB particles. However, the cyclability of this cell was not so good, reaching 64 mAh/g<sub>S</sub> at discharge at 0.1 C after 65 cycles of discharge–charge. The reason for this was thought to be the migration of sulfides towards the inner cathode surface facing the separator and the formation of deposits there. Future research efforts need to focus on further slowing down the rate of sulfide migration through the cathode.

**Supplementary Materials:** The following supporting information can be downloaded at: <https://www.mdpi.com/article/10.3390/batteries10060216/s1>, Figure S1: Specific capacity at discharge versus cycle number in the galvanostatic discharge-charge tests at different C-rates of Na-S cells with cathode of 44 wt% sulfur with host AC MSC 30, for all six electrolytes and different E/S ratios (in ml/mgS): (a) 1M NaTFSI in DOL/DME; (b) 1M NaTFSI in TEGDME; (c) 1M NaFSI in DOL/DME; (d) 1M NaFSI in TEGDME; (e) 1M NaCF<sub>3</sub>SO<sub>3</sub> in DOL/DME; (f) 1M NaCF<sub>3</sub>SO<sub>3</sub> in TEGDME. Figure S2: Photos of Na-S cell components, postmortem after cycling (65 cycles) and electrochemical testing: A = anode, S = separator (surface facing cathode), C = cathode. (a) Na-S cell with electrolyte 1 M NaTFSI in DOL/DME at three E/S ratios; (b) Na-S cell with electrolyte 1 M NaTFSI in TEGDME at three E/S ratios. Figure S3: Photos of Na-S cell components, postmortem after cycling (65 cycles) and electrochemical testing: A = anode, S = separator (surface facing cathode), C = cathode. (a) Na-S cell with electrolyte 1 M NaFSI in DOL/DME at three E/S ratios; (b) Na-S cell with electrolyte 1 M NaFSI in TEGDME at three E/S ratios. Figure S4: Photos of Na-S cell components, postmortem after cycling (65 cycles) and electrochemical testing: A = anode, S = separator (surface facing cathode), C = cathode. (a) Na-S cell with electrolyte 1 M NaCF<sub>3</sub>SO<sub>3</sub> in DOL/DME at three E/S ratios; (b) Na-S cell with electrolyte 1 M NaCF<sub>3</sub>SO<sub>3</sub> in TEGDME at three E/S ratios.

**Author Contributions:** Conceptualization, H.A.A. and C.L.; methodology, H.A.A., S.T., J.F.W. and C.L.; formal analysis, H.A.A. and C.L.; investigation, H.A.A.; resources, C.L. and J.F.W.; data curation, H.A.A. and C.L.; writing—original draft preparation, H.A.A.; writing—review and editing, H.A.A., S.T., J.F.W. and C.L.; visualization, H.A.A.; supervision, C.L., S.T. and J.F.W.; project administration, C.L. All authors have read and agreed to the published version of the manuscript.

**Funding:** This research received no external funding.

**Data Availability Statement:** All data are made available in this study. Any further data will become available after reasonable request.

**Conflicts of Interest:** The authors declare no conflicts of interest.

## References

1. Chen, K.; Zhao, F.; Hao, H.; Liu, Z. Selection of Li-ion battery technologies for electric vehicles under China's new energy vehicle credit regulation. *Energy Procedia* **2019**, *158*, 3038–3044. [[CrossRef](#)]
2. Najera, J.; Arribas, J.R.; de Castro, R.M.; Nunez, C.S. Semi-empirical ageing model for LFP and NMC Li-ion battery chemistries. *J. Energy Storage A* **2023**, *72*, 108016. [[CrossRef](#)]
3. Sanad, M.M.S.; Meselhy, N.K.; El-Boraey, H.A. Surface protection of NMC811 cathode material via ZnSnO<sub>3</sub> perovskite film for enhanced electrochemical performance in rechargeable Li-ion batteries. *Colloids Surf. A-Physicochem. Eng. Asp.* **2023**, *672*, 131748. [[CrossRef](#)]
4. Minnetti, L.; Marangon, V.; Andreotti, P.; Staffolani, A.; Nobili, F.; Hassoun, J. Reciprocal irreversibility compensation of LiNi<sub>0.2</sub>Co<sub>0.2</sub>Al<sub>0.1</sub>Mn<sub>0.45</sub>O<sub>2</sub> cathode and silicon oxide anode in new Li-ion battery. *Electrochim. Acta* **2023**, *452*, 142263. [[CrossRef](#)]
5. Nguyen, T.T.; Nguyen, N.Q.; Thai, D.; Tieu, T.D.; Tran, V.; Le, M.L.P. Enabling stable and high-rate of an olivine-type cathode LiFePO<sub>4</sub> for Li-ion batteries by using graphene nanoribbons as conductive agent. *Adv. Nat. Sci.-Nanosci. Nanotechnol.* **2023**, *14*, 015009. [[CrossRef](#)]
6. Chen, L.Y.; Chiang, C.L.; Wu, X.H.; Tang, Y.L.; Zeng, G.F.; Zhou, S.Y.; Zhang, B.D.; Zhang, H.T.; Yan, Y.W.; Liu, T.T.; et al. Prolonged lifespan of initial-anode-free lithium-metal battery by pre-lithiation in Li-rich Li<sub>2</sub>Ni<sub>0.5</sub>Mn<sub>1.5</sub>O<sub>4</sub> spinel cathode. *Chem. Sci.* **2023**, *14*, 2183–2191. [[CrossRef](#)] [[PubMed](#)]
7. Choi, D.; Kwon, H.; Lim, S.; Jeong, T.; Jung, H.C.; Kim, Y.I.; Han, D.W. Unexplored orthorhombic LiMn<sub>1-x</sub>Ti<sub>x</sub>O<sub>2</sub> cathode materials with a stable atomic site occupancy and phase transition. *Energy Fuels* **2023**, *37*, 1404–1413. [[CrossRef](#)]
8. Lin, K.; Xu, X.; Qin, X.; Liu, M.; Zhao, L.; Yang, Z.; Liu, Q.; Ye, Y.; Chen, G.; Kang, F.; et al. Batteries with high energy density realized by symbiotic anode and prelithiated cathode. *Nano-Micro Lett.* **2022**, *14*, 149. [[CrossRef](#)]
9. Kang, J.; Atwair, M.; Nam, I.; Lee, C.J. Experimental and numerical investigation on effects of thickness of NCM622 cathode in Li-ion batteries for high energy and power density. *Energy* **2022**, *263*, 125801. [[CrossRef](#)]
10. Singh, S.K.; Dutta, D.P.; Gupta, H.; Srivastava, N.; Mishra, R.; Meghni, D.; Tiwari, R.K.; Patel, A.; Tiwari, A.; Singh, R.K. Electrochemical investigation of double layer surface-functionalized Li-NMC cathode with nano-composite gel polymer electrolyte for Li-battery applications. *Electrochim. Acta* **2022**, *435*, 141328. [[CrossRef](#)]
11. Zhu, K.; Wang, C.; Chi, Z.; Ke, F.; Yang, Y.; Wang, A.; Wang, W.; Miao, L. How far away are lithium-sulfur batteries from commercialization? *Frontiers* **2019**, *7*, 00123. [[CrossRef](#)]
12. Fei, Y.; Li, G. Unveiling the pivotal parameters for advancing high energy density in lithium-sulfur batteries: A comprehensive review. *Adv. Funct. Mater.* **2024**, *34*, 2312550. [[CrossRef](#)]
13. Zhao, M.; Peng, H.-J.; Li, B.-Q.; Huang, J.-Q. Kinetic promoters for sulfur cathodes in lithium-sulfur batteries. *Acc. Chem. Res.* **2024**, *57*, 545–557. [[CrossRef](#)] [[PubMed](#)]
14. Brieske, D.M.; Warnecke, A.; Sauer, D.U. Modeling the volumetric expansion of the lithium-sulfur battery considering charge and discharge profiles. *Energy Storage Mater.* **2023**, *55*, 289–300. [[CrossRef](#)]
15. Shaibani, M.; Mirshekarloo, M.S.; Singh, R.; Easton, C.D.; Cooray, M.C.D.; Eshraghi, N.; Abendroth, T.; Dörfler, S.; Holger Althues, H.; Kaskel, S.; et al. Expansion-tolerant architectures for stable cycling of ultrahigh-loading sulfur cathodes in lithium-sulfur batteries. *Sci. Adv.* **2020**, *6*, eaay2757. [[CrossRef](#)]
16. Grabe, S.; Dent, M.; Zhang, T.; Tennison, S.; Lekakou, C. A physicochemical model-based digital twin of Li-S batteries to elucidate the effects of cathode microstructure and evaluate different microstructures. *J. Power Sources* **2023**, *580*, 233470. [[CrossRef](#)]
17. He, G.; Evers, S.; Liang, X.; Cuisinier, M.; Garsuch, A.; Nazar, L.F. Tailoring porosity in carbon nanospheres for lithium-sulfur battery cathodes. *ACS Nano* **2013**, *7*, 10920–10930. [[CrossRef](#)] [[PubMed](#)]
18. Lai, X.X.; Fan, K.B.; Zhang, Z.Q.; Cai, L.L.; Zhu, Z.H.; Huang, H.Z.; Zhang, Q.S.; Sun, L.; Zhou, Z.H.; Wang, L.; et al. Cobalt hydroxide decorating N-doped hollow carbon sphere as a new sulfur host to improve long cycle stability in lithium-sulfur batteries. *Ioniczangs* **2024**, online. [[CrossRef](#)]
19. Lu, W.; Wang, L.; Han, C.; Chao, Y.; Xu, C.; Zhu, J.; Tian, Y.; Wang, Z.; Cui, X. MoP quantum dots based multifunctional efficient electrocatalyst for stable and long-life flexible lithium-sulfur batteries. *J. Colloid Interface Sci.* **2024**, *661*, 83–90. [[CrossRef](#)]
20. Lu, X.; Meng, Y.S.; Wang, X.; Xiao, M.J.; Xu, Y.S.; Zhu, F.L. Preparation of NiCo<sub>2</sub>S<sub>4</sub>/carbon hollow sphere for long cycle lithium sulfur batteries. *J. Mater. Sci. Mater. Electron.* **2024**, *35*, 83. [[CrossRef](#)]
21. Zang, J.; An, T.; Dong, Y.; Fang, X.; Zheng, M.; Dong, Q.; Zheng, N. Hollow-in-hollow carbon spheres with hollow foam-like cores for lithium-sulfur batteries. *Nano Res.* **2015**, *8*, 2663–2675. [[CrossRef](#)]
22. Li, B.; Xie, M.; Yia, G.; Zhang, C. Biomass-derived activated carbon/sulfur composites as cathode electrodes for Li-S batteries by reducing the oxygen content. *RSC Adv.* **2020**, *10*, 2823–2829. [[CrossRef](#)]
23. Moreno, N.; Caballero, A.; Hernán, L.; Morales, J. Lithium-sulfur batteries with activated carbons derived from olive stones. *Carbon* **2014**, *70*, 241–248. [[CrossRef](#)]
24. Pozio, A.; Di Carli, M.; Aurora, A.; Falconieri, M.; Seta, L.D.; Prosini, P.P. Hard carbons for use as electrodes in Li-S and Li-ion batteries. *Nanomaterials* **2022**, *12*, 1349. [[CrossRef](#)]
25. Lama, F.L.; Marangon, V.; Caballero, A.; Morales, J.; Hassoun, J. Diffusional features of a lithium-sulfur battery exploiting highly microporous activated carbon. *ChemSusChem* **2023**, *16*, e202202095. [[CrossRef](#)]
26. Bora, M.; Bhattacharjya, D.; Saikia, B.K. Coal-derived activated carbon for electrochemical energy storage: Status on supercapacitor, Li-ion battery, and Li-S battery applications. *Energy Fuels* **2021**, *35*, 18285–18307. [[CrossRef](#)]

27. Zhang, S.; Zheng, M.; Lin, Z.; Li, N.; Liu, Y.; Zhao, B.; Pang, H.; Cao, J.; Hea, P.; Shi, Y. Activated carbon with ultrahigh specific surface area synthesized from natural plant material for lithium–sulfur batteries. *J. Mater. Chem. A* **2014**, *2*, 15889–15896. [[CrossRef](#)]
28. Tonoya, T.; Ando, H.; Takeichi, N.; Senoh, H.; Kojima, T.; Hinago, H.; Matsui, Y.; Ishikawa, M. Capacity decay mechanism of lithium–sulfur batteries using a microporous activated carbon–sulfur composite as the cathode material. *J. Phys. Chem. C* **2023**, *127*, 10038–10044. [[CrossRef](#)]
29. Fields, R.; Lei, C.; Markoulidis, F.; Lekakou, C. The composite supercapacitor. *Energy Technol.* **2016**, *4*, 517–525. [[CrossRef](#)]
30. Lei, C.; Fields, R.; Wilson, P.; Lekakou, C.; Amini, N.; Tennison, S.; Perry, J.; Gosso, M.; Martorana, B. Development and evaluation of a composite supercapacitor-based 12 V transient start–stop power system for vehicles: Modelling, design and fabrication scaling up. *Proc. Inst. Mech. Eng. Part A* **2021**, *235*, 914–927. [[CrossRef](#)]
31. Markoulidis, F.; Lei, C.; Lekakou, C. Investigations of activated carbon fabric-based supercapacitors with different interlayers via experiments and modelling of electrochemical processes of different timescales. *Electrochim. Acta* **2017**, *249*, 122–134. [[CrossRef](#)]
32. Elazari, R.; Salitra, G.; Garsuch, A.; Panchenko, A.; Aurbach, D. Sulfur-impregnated activated carbon fiber cloth as a binder-free cathode for rechargeable Li-S batteries. *Adv. Mater.* **2011**, *23*, 5641–5644. [[CrossRef](#)]
33. Swiderska-Mocek, A.; Rudnicka, E. Lithium–sulphur battery with activated carbon cloth–sulphur cathode and ionic liquid as electrolyte. *J. Power Sources* **2015**, *273*, 162–167. [[CrossRef](#)]
34. He, N.; Zhong, L.; Xiao, M.; Wang, S.; Han, D.; Meng, Y. Foldable and high sulfur loading 3D carbon electrode for high-performance Li-S battery application. *Sci. Rep.* **2016**, *6*, 33871. [[CrossRef](#)]
35. Brehm, W.; Marangon, V.; Panda, J.; Thorat, S.B.; del Rio Castillo, A.E.; Bonaccorso, F.; Pellegrini, V.; Hassoun, J. A Lithium–sulfur battery using binder-free graphene-coated aluminum current collector. *Energy Fuels* **2022**, *36*, 9321–9328. [[CrossRef](#)]
36. Zhang, Y.; Gao, Z.; Song, N.; He, J.; Li, X. Graphene and its derivatives in lithium–sulfur batteries. *Mater. Today Energy* **2018**, *9*, 319–335. [[CrossRef](#)]
37. Yang, T.; Xia, J.; Piao, Z.; Yang, L.; Zhang, S.; Xing, Y.; Zhou, G. Graphene-based materials for flexible lithium–sulfur batteries. *ACS Nano* **2021**, *15*, 13901–13923. [[CrossRef](#)]
38. Tian, J.; Xing, F.; Gao, Q. Graphene-based nanomaterials as the cathode for lithium–sulfur batteries. *Molecules* **2021**, *26*, 2507. [[CrossRef](#)]
39. Kim, H.; Lim, H.-D.; Kima, J.; Kang, K. Graphene for advanced Li/S and Li/air batteries. *J. Mater. Chem. A* **2014**, *2*, 33–47. [[CrossRef](#)]
40. Ji, L.; Rao, M.; Zheng, H.; Zhang, L.; Li, Y.; Duan, W.; Guo, J.; Cairns, E.J.; Zhang, Y. Graphene oxide as a sulfur immobilizer in high performance lithium/sulfur cells. *J. ACS* **2011**, *133*, 18522–18525. [[CrossRef](#)] [[PubMed](#)]
41. Reece, R.; Lekakou, C.; Smith, P.A.; Grilli, R.; Trapalis, C. Sulphur-linked graphitic and graphene oxide platelet-based electrodes for electrochemical double layer capacitors. *J. Alloys Compd.* **2019**, *792*, 582–593. [[CrossRef](#)]
42. Baboo, J.P.; Babar, S.; Kale, D.; Lekakou, C.; Laudone, G.M. Designing a graphene coating-based supercapacitor with lithium ion electrolyte: An experimental and computational study via multiscale modeling. *Nanomaterials* **2021**, *11*, 2899. [[CrossRef](#)]
43. Vermisoglou, E.C.; Giannakopoulou, T.; Romanos, G.; Boukos, N.; Psycharis, V.; Lei, C.; Lekakou, C.; Petridis, D.; Trapalis, C. Graphene-based materials via benzidine-assisted exfoliation and reduction of graphite oxide and their electrochemical properties. *Appl. Surf. Sci.* **2017**, *392*, 244–255. [[CrossRef](#)]
44. Doñoro, A.; Muñoz-Mauricio, A.; Etacheri, V. High-Performance lithium sulfur batteries based on multidimensional graphene-CNT-nanosulfur hybrid cathodes. *Batteries* **2021**, *7*, 26. [[CrossRef](#)]
45. Zheng, M.; Chi, Y.; Hu, Q.; Tang, H.; Jiang, X.; Zhang, L.; Zhang, S.; Pang, H.; Xu, Q. Carbon nanotube-based materials for lithium–sulfur batteries. *J. Mater. Chem. A* **2019**, *7*, 17204–17241. [[CrossRef](#)]
46. Yahalom, N.; Snarski, L.; Maity, A.; Bendikov, T.; Leskes, M.; Weissman, H.; Rybtchinski, B. Durable lithium–sulfur batteries based on a composite carbon nanotube cathode. *ACS Appl. Energy Mater.* **2023**, *6*, 4511–4519. [[CrossRef](#)]
47. Yoshie, Y.; Hori, K.; Mae, T.; Noda, S. High-energy-density Li–S battery with positive electrode of lithium polysulfides held by carbon nanotube sponge. *Carbon* **2021**, *182*, 32–41. [[CrossRef](#)]
48. Zhu, S.; Sheng, J.; Chen, Y.; Ni, J.; Li, Y. Carbon nanotubes for flexible batteries: Recent progress and future perspective. *Natl. Sci. Rev.* **2021**, *8*, nwaa261. [[CrossRef](#)]
49. Ma, L.; Zhuang, H.L.; Wei, S.; Hendrickson, K.E.; Kim, M.S.; Cohn, G.; Hennig, R.G.; Archer, L.A. Enhanced Li–S batteries using amine-functionalized carbon nanotubes in the cathode. *ACS Nano* **2016**, *10*, 1050–1059. [[CrossRef](#)]
50. Murugesu, A.K.; Uthayanan, A.; Lekakou, C. Electrophoresis and orientation of multiple wall carbon nanotubes in polymer solution. *Appl. Phys. A* **2010**, *100*, 135–144. [[CrossRef](#)]
51. Yu, B.; Chen, Y.; Wang, Z.; Chen, D.; Wang, X.; Zhang, W.; He, J.; He, W. 1T-MoS<sub>2</sub> nanotubes wrapped with N-doped graphene as highly-efficient absorbent and electrocatalyst for Li–S batteries. *J. Power Sources* **2020**, *447*, 227364. [[CrossRef](#)]
52. Li, M.; Sami, I.; Yang, J.; Li, J.; Kumar, R.V.; Chhowalla, M. Lithiated metallic molybdenum disulfide nanosheets for high-performance lithium–sulfur batteries. *Nat. Energy* **2023**, *8*, 84–93. [[CrossRef](#)]
53. Hojaji, E.; Andritsos, E.I.; Li, Z.; Chhowalla, M.; Lekakou, C.; Cai, Q. DFT Simulation-based design of 1T-MoS<sub>2</sub> cathode hosts for Li-S batteries and experimental evaluation. *Int. J. Mol. Sci.* **2022**, *23*, 15608. [[CrossRef](#)] [[PubMed](#)]
54. Andritsos, E.I.; Lekakou, C.; Cai, Q. Single-atom catalysts as promising cathode materials for lithium–sulfur batteries. *J. Phys. Chem. C* **2021**, *125*, 18108–18118. [[CrossRef](#)]

55. Zhou, G.; Zhao, S.; Wang, T.; Yang, S.-Z.; Johannessen, B.; Chen, H.; Liu, C.; Ye, Y.; Wu, Y.; Peng, Y.; et al. Theoretical calculation guided design of single-atom catalysts toward fast kinetic and long-life Li-S batteries. *Nano Lett.* **2020**, *20*, 1252–1261. [[CrossRef](#)]
56. Wang, K.; Liu, S.; Shu, Z.; Zheng, Q.; Zheng, M.; Dong, Q. Single-atom site catalysis in Li-S batteries. *Phys. Chem. Chem. Phys.* **2023**, *25*, 25942–25960. [[CrossRef](#)] [[PubMed](#)]
57. Zhou, T.; Liang, J.; Ye, S.; Zhang, Q.; Liu, J. Fundamental, application and opportunities of single atom catalysts for Li-S batteries. *Energy Storage Mater.* **2023**, *55*, 322–355. [[CrossRef](#)]
58. Sun, X.; Qiu, Y.; Jiang, B.; Chen, Z.; Zhao, C.; Zhou, H.; Yang, L.; Fan, L.; Zhang, Y.; Zhang, N. Isolated Fe-Co heteronuclear diatomic sites as efficient bifunctional catalysts for high-performance lithium-sulfur batteries. *Nat. Commun.* **2023**, *14*, 291. [[CrossRef](#)]
59. Grabe, S.; Dent, M.; Babar, S.; Zhang, T.; Tennison, S.; Watts, J.F.; Lekakou, C. Investigation and Determination of Electrochemical Reaction Kinetics in Lithium-Sulfur Batteries with Electrolyte LiTFSI in DOL/DME. *J. Electrochem. Soc.* **2023**, *170*, 020527. [[CrossRef](#)]
60. Li, H.; Lampkin, J.; Garcia-Araez, N. Facilitating charge reactions in Al-S batteries with redox mediators. *ChemSusChem* **2021**, *14*, 3139–3146. [[CrossRef](#)]
61. Klimpel, M.; Kovalenko, M.V.; Kravchyk, K.V. Advances and challenges of aluminum-sulfur batteries. *Commun. Chem.* **2022**, *5*, 77. [[CrossRef](#)] [[PubMed](#)]
62. Li, R.; Liu, Q.; Zhang, R.; Li, Y.; Ma, Y.; Huo, H.; Gao, Y.; Zuo, P.; Wang, J.; Yin, G. Achieving high-energy-density magnesium/sulfur battery via a passivation-free Mg-Li alloy anode. *Energy Storage Mater.* **2022**, *50*, 380–386. [[CrossRef](#)]
63. Li, Z.; Vinayan, B.P.; Diemant, T.; Behm, R.J.; Fichtner, M.; Zhao-Karger, Z. Rechargeable calcium-sulfur batteries enabled by an efficient borate-based electrolyte. *Small* **2020**, *16*, 2001806. [[CrossRef](#)]
64. Nikiforidis, G.; van de Sanden, M.C.M.; Tsampas, M.N. High and intermediate temperature sodium-sulfur batteries for energy storage: Development, challenges and perspectives. *RSC Adv.* **2019**, *9*, 5649–5673. [[CrossRef](#)]
65. Liang, Y.; Zhang, B.; Shi, Y.; Jiang, R.; Zhang, H. Research on wide-temperature rechargeable sodium-sulfur batteries: Features, challenges and solutions. *Materials* **2023**, *16*, 4263. [[CrossRef](#)] [[PubMed](#)]
66. Vudata, S.P.; Bhattacharyya, D. Thermal management of a high temperature sodium sulphur battery stack. *Int. J. Heat and Mass Transf.* **2021**, *181*, 122025. [[CrossRef](#)]
67. Antonano, H.C.; Panganiban, J.M.F.; Yu, J.V.T.; Castro, M.T.; Ocon, J.D. Multiphysics modeling of high temperature planar sodium-sulfur batteries. *Chem. Eng. Trans.* **2022**, *94*, 1093–1098.
68. Hueso, K.; Armand, M.; Rojo, T. High temperature sodium batteries: Status, challenges and future trends. *Energy Environ. Sci.* **2013**, *6*, 734–749. [[CrossRef](#)]
69. Dent, M.; Jakubczyk, E.; Zhang, T.; Lekakou, C. Kinetics of sulphur dissolution in lithium-sulphur batteries. *J. Phys. Energy* **2022**, *4*, 024001. [[CrossRef](#)]
70. Li, G.; Li, Z.; Zhang, B.; Lin, Z. Developments of electrolyte systems for lithium-sulfur batteries: A review. *Front. Energy Res.* **2015**, *3*, 00005. [[CrossRef](#)]
71. Gao, J.; Lowe, M.A.; Kiya, Y.; Abruña, H.D. Effects of liquid electrolytes on the charge-discharge performance of rechargeable lithium/sulfur batteries: Electrochemical and in-situ X-ray absorption spectroscopic studies. *J. Phys. Chem. C* **2011**, *115*, 25132–25137. [[CrossRef](#)]
72. Yin, T.; Park, M.-S.; Yu, J.-S.; Kim, K.J.; Im, K.Y.; Kim, J.-H.; Jeong, G.; Jo, Y.N.; Woo, S.-G.; Kang, K.S.; et al. Effect of chemical reactivity of polysulfide toward carbonate-based electrolyte on the electrochemical performance of Li-S batteries. *Electrochim. Acta* **2013**, *107*, 454–460. [[CrossRef](#)]
73. He, M.; Li, X.; Yang, X.; Wang, C.; Zheng, M.L.; Li, R.; Zuo, P.; Yin, G.; Sun, X. Realizing solid-phase reaction in Li-S batteries via localized high-concentration carbonate electrolyte. *Adv. Energy Mater.* **2021**, *11*, 2101004. [[CrossRef](#)]
74. Rafie, A.; Kim, J.W.; Sarode, K.K.; Kalra, V. A review on the use of carbonate-based electrolytes in Li-S batteries: A comprehensive approach enabling solid-solid direct conversion reaction. *Energy Storage Mater.* **2022**, *50*, 197–224. [[CrossRef](#)]
75. Li, X.; Banis, M.; Lushington, A.; Yang, X.; Sun, Q.; Zhao, Y.; Liu, C.; Li, Q.; Wang, B.; Xiao, W.; et al. A high-energy sulfur cathode in carbonate electrolyte by eliminating polysulfides via solid-phase lithium-sulfur transformation. *Nat. Commun.* **2018**, *9*, 4509. [[CrossRef](#)]
76. Syali, M.S.; Kumar, D.; Mishra, K.; Kanchan, D.K. Recent advances in electrolytes for room-temperature sodium-sulfur batteries: A review. *Energy Storage Mater.* **2020**, *31*, 352–372. [[CrossRef](#)]
77. Wei, S.; Xu, S.; Agrawal, A.; Choudhury, S.; Lu, Y.; Tu, Z.; Ma, L.; Archer, L.A. A stable room-temperature sodium-sulfur battery. *Nat. Comm.* **2016**, *7*, 11722. [[CrossRef](#)] [[PubMed](#)]
78. Wang, N.; Wang, Y.; Bai, Z.; Fang, Z.; Zhang, X.; Xu, Z.; Ding, Y.; Xu, X.; Du, Y.; Dou, S.; et al. High-performance room-temperature sodium-sulfur battery enabled by electrocatalytic sodium polysulfides full conversion. *Energy Environ. Sci.* **2020**, *13*, 562–570. [[CrossRef](#)]
79. Chen, P.; Wang, C.; Wang, T. Review and prospects for room-temperature sodium-sulfur batteries. *Mater. Res. Lett.* **2022**, *10*, 691–719. [[CrossRef](#)]
80. Wang, L.; Wang, T.; Peng, L.; Wang, Y.; Zhang, M.; Zhou, J.; Chen, M.; Cao, J.; Fei, H.; Duan, X.; et al. The promises, challenges and pathways to room-temperature sodium-sulfur batteries. *Natl. Sci. Rev.* **2022**, *9*, nwab050. [[CrossRef](#)]
81. Adeoye, H.A.; Dent, M.; Watts, J.F.; Tennison, S.; Lekakou, C. Solubility and dissolution kinetics of sulfur and sulfides in electrolyte solvents for lithium-sulfur and sodium-sulfur batteries. *J. Chem. Phys.* **2023**, *158*, 064702. [[CrossRef](#)] [[PubMed](#)]



82. Bates, J.; Markoulidis, F.; Lekakou, C.; Laudone, C.M. Design of porous carbons for supercapacitor applications for different organic solvent-electrolytes. *C* **2021**, *7*, 15. [[CrossRef](#)]
83. Markoulidis, F.; Bates, J.; Lekakou, C.; Slade, R.; Laudone, G.M. Supercapacitors with lithium-ion electrolyte: An experimental study and design of the activated carbon electrodes via modelling and simulations. *Carbon* **2020**, *164*, 422–434. [[CrossRef](#)]
84. Lasetta, K.; Baboo, J.P.; Lekakou, C. Modeling and simulations of the sulfur infiltration in activated carbon fabrics during composite cathode fabrication for lithium-sulfur batteries. *J. Compos. Sci.* **2021**, *5*, 65. [[CrossRef](#)]
85. Grabe, S.; Baboo, J.P.; Tennison, S.; Zhang, T.; Lekakou, C.; Andritsos, E.I.; Cai, Q.; Downes, S.; Hinder, S.; Watts, J.F. Sulfur infiltration and allotrope formation in porous cathode hosts for lithium-sulfur batteries. *AIChE J.* **2022**, *68*, e17638. [[CrossRef](#)]
86. Li, Y.; Fu, K.; Chen, C.; Luo, W.; Gao, T.; Xu, S.; Dai, J.; Pastel, G.; Wang, Y.; Liu, B.; et al. Enabling high-areal-capacity lithium-sulfur batteries: Designing anisotropic and low-tortuosity porous architectures. *ACS Nano* **2017**, *11*, 4801–4807. [[CrossRef](#)]
87. Feng, S.; Singh, R.K.; Fu, Y.; Li, Z.; Wang, Y.; Bao, J.; Xu, Z.; Li, G.; Anderson, C.; Shi, L.; et al. Low-tortuous and dense single-particle-layer electrode for high-energy lithium-sulfur batteries. *Energy Environ. Sci.* **2022**, *15*, 3842–3853. [[CrossRef](#)]
88. Babar, S.; Lekakou, C. Molecular modeling of electrolyte and polysulfide ions for lithium-sulfur batteries. *Ionics* **2021**, *27*, 635–642. [[CrossRef](#)]
89. Sdanghi, G.; Schaefer, S.; Maranzana, G.; Celzard, A.; Fierro, V. Application of the modified Dubinin-Astakhov equation for a better understanding of high-pressure hydrogen adsorption on activated carbons. *Int. J. Hydrog. Energy* **2020**, *45*, 25912–25926. [[CrossRef](#)]
90. Kannan, D.R.R.; Terala, P.K.; Moss, P.L.; Weatherspoon, M.H. Analysis of the separator thickness and porosity on the performance of lithium-ion batteries. *Int. J. Electrochem.* **2018**, *2018*, 1925708.
91. Zhou, Y.-T.; Yang, J.; Liang, H.-Q.; Pi, J.-K.; Zhang, C.; Xu, Z.-K. Sandwich-structured composite separators with an anisotropic pore architecture for highly safe Li-ion batteries. *Compos. Commun.* **2018**, *8*, 46–51. [[CrossRef](#)]
92. Jang, J.; Oh, J.; Jeong, H.; Kang, W.; Jo, C. A review of functional separators for lithium metal battery applications. *Materials* **2020**, *13*, 4625. [[CrossRef](#)]
93. Baboo, J.P.; Jakubczyk, E.; Yattoo, M.A.; Phillips, M.; Grabe, S.; Dent, M.; Hinder, S.J.; Watts, J.F.; Lekakou, C. Investigating battery-supercapacitor material hybrid configurations in energy storage device cycling at 0.1 to 10C rate. *J. Power Sources* **2023**, *561*, 232762. [[CrossRef](#)]
94. Baboo, J.P.; Yattoo, M.A.; Dent, M.; Hojaji Najafabadi, E.; Lekakou, C.; Slade, R.; Hinder, S.J.; Watts, J.F. Exploring different binders for a LiFePO<sub>4</sub> battery, battery testing, modeling and simulations. *Energies* **2022**, *15*, 2332. [[CrossRef](#)]
95. Dent, M.; Grabe, S.; Lekakou, C. The challenge of electrolyte impregnation in the fabrication and operation of Li-ion and Li-S batteries. *Batter. Supercaps* **2024**, *7*, e202300327. [[CrossRef](#)]
96. Guo, Q.; Sun, S.; Kim, K.; Zhang, H.; Liu, X.; Yan, C.; Xia, H. A novel one-step reaction sodium-sulfur battery with high areal sulfur loading on hierarchical porous carbon fiber. *Carbon Energy* **2021**, *3*, 440–448. [[CrossRef](#)]
97. Yan, Z.; Zhao, L.; Wang, Y.; Zhu, Z.; Chou, S.-L. The future for room-temperature sodium-sulfur batteries: From persisting issues to promising solutions and practical applications. *Adv. Funct. Mater.* **2022**, *32*, 2205622. [[CrossRef](#)]
98. Kumar, D.; Rajouria, S.K.; Kuhar, S.B.; Kanchan, D.K. Progress and prospects of sodium-sulfur batteries: A review. *Solid State Ion.* **2017**, *312*, 8–16. [[CrossRef](#)]
99. Xu, X.; Zhou, D.; Qin, X.; Lin, K.; Kang, F.; Li, B.; Shanmukaraj, D.; Rojo, T.; Armand, M.; Wang, G. A room-temperature sodium-sulfur battery with high capacity and stable cycling performance. *Nat. Commun.* **2018**, *9*, 3870. [[CrossRef](#)]
100. Pham, T.D.; Bin Faheem, A.; Kim, J.; Oh, H.M.; Lee, K.-K. Practical high-voltage lithium metal batteries enabled by tuning the solvation structure in weakly solvating electrolyte. *Small* **2022**, *18*, 2107492. [[CrossRef](#)]
101. Safari, M.; Kwok, C.Y.; Nazar, L.F. Transport properties of polysulfide species in lithium-sulfur battery electrolytes: Coupling of experiment and theory. *ACS Cent. Sci.* **2016**, *2*, 560–568. [[CrossRef](#)] [[PubMed](#)]
102. Wenzel, S.; Metelmann, H.; Raiß, C.; Dürr, A.K.; Janek, J.; Adelhelm, P. Thermodynamics and cell chemistry of room temperature sodium/sulfur cells with liquid and liquid/solid electrolyte. *J. Power Sources* **2013**, *243*, 758–765. [[CrossRef](#)]
103. Kim, K.-M.; Hur, J.-W.; Jung, S.; Kang, A.-S. Electrochemical characteristics of activated carbon/Ppy electrode combined with P(VdF-co-HFP)/PVP for EDLC. *Electrochim. Acta* **2004**, *50*, 863–872. [[CrossRef](#)]
104. Kim, I.; Park, J.-Y.; Kim, C.H.; Park, J.-W.; Ahn, J.-P.; Ahn, J.-H.; Kim, K.-W.; Ahn, H.-J. Sodium polysulfides during charge/discharge of the room-temperature Na/S battery using TEGDME electrolyte. *J. Electrochem. Soc.* **2016**, *163*, A611–A616. [[CrossRef](#)]
105. Liu, H.; Lai, W.-H.; Lei, Y.; Yang, H.; Wang, N.; Chou, S.; Liu, H.K.; Dou, S.X.; Wang, Y.-X. Electrolytes/interphases: Enabling distinguishable sulfur redox processes in room-temperature sodium-sulfur batteries. *Adv. Energy Mater.* **2022**, *12*, 2103304. [[CrossRef](#)]
106. Shi, C.; Takeuchi, S.; Alexander, G.V.; Hamann, T.; O'Neill, J.; Dura, J.A.; Wachsman, E.D. High sulfur loading and capacity retention in bilayer garnet sulfurized-polyacrylonitrile/lithium-metal batteries with gel polymer electrolytes. *Adv. Energy Mater.* **2023**, *13*, 2301656. [[CrossRef](#)]
107. Hwang, T.H.; Jung, D.S.; Kim, J.-S.; Kim, B.G.; Choi, J.W. One-dimensional carbon-sulfur composite fibers for Na-S rechargeable batteries operating at room temperature. *Nano Lett.* **2013**, *13*, 4532–4538. [[CrossRef](#)]

**Disclaimer/Publisher's Note:** The statements, opinions and data contained in all publications are solely those of the individual author(s) and contributor(s) and not of MDPI and/or the editor(s). MDPI and/or the editor(s) disclaim responsibility for any injury to people or property resulting from any ideas, methods, instructions or products referred to in the content.